Contents lists available at ScienceDirect

Remote Sensing of Environment

journal homepage: www.elsevier.com/locate/rse

Detection of inland water bodies under dense biomass by CYGNSS

Hugo Carreno-Luengo [a,*], Christopher S. Ruf [a], Scott Gleason [b], Anthony Russel [a]

[a] Climate and Space Sciences and Engineering Department, University of Michigan (UMich), Ann Arbor, MI, USA
[b] Daaxa LLC, Boulder, CO, USA

ARTICLE INFO

Edited by Menghua Wang

Keywords:
CYGNSS
GNSS-R
Inland water bodies
Biomass
Coherent scattering
Methane emissions

ABSTRACT

The reliable detection of inland water bodies under dense biomass is not possible with traditional spaceborne remote sensing systems. In this investigation, we demonstrate the capability of the National Aeronautics and Space Administration (NASA) Cyclone Global Navigation Satellite System (CYGNSS) mission to detect and quantify the extent of small water bodies under dense biomass up to 400 ton/ha in complex heterogenous scenes such as tropical rainforests. A novel inland water body product based on L1 CYGNSS data is developed using a combination of peak surface reflectivity Γ_p and its spread with respect to time delay and Doppler shift, as characterized by the power ratio P_{ratio}. Only L1 CYGNSS mission data has the potential to study Earth's surface water dynamics because raw Intermediate Frequency (IF) data availability is limited. Several coherence indices are used to verify that the L-band Global Positioning System (GPS) signals are being coherently reflected by surface water bodies and attenuated by the intervening vegetation canopy. These indices include full and computationally fast versions of the entropy associated with Delay Doppler Maps (DDMs), E_{full} and E_{fast}, as well as the time derivative of the phase φ_{peak} of the reflected GPS signal. The capability to accurately resolve surface water extent under dense vegetation has been shown to improve the estimation by current state-of-art surface water extension datasets used by global methane CH4 emission models in wetlands.

1. Introduction

The detection of inland water bodies is an important new scientific application of the NASA CYGNSS mission (Ruf et al., 2013; Ruf et al., 2015). Monitoring highly dynamic surface water extent requires high spatio-temporal sampling observations with high spatial resolution. CYGNSS can generate such measurements independently of weather conditions, using surface reflected L-band GPS signals as signals-of-opportunity (Ruf et al., 2018; Morris et al., 2019; Gerlein-Safdi et al., 2021; Al-Khaldi et al., 2021; Downs et al., 2023; Chew et al., 2023). This technique is known as Global Navigation Satellite Systems Reflectometry (GNSS-R) (Martín-Neira, 1993; Garrison and Katzberg, 2000; Lowe et al., 2002; Camps, 2021; Zavorotny et al., 2014; Wickert et al., 2016; Cardellach et al., 2018; Pierdicca et al., 2021), which is essentially an L-band passive multi-bistatic radar. GNSS-R uses the existing navigation satellites which are in view as signal transmitters. Consequently, spaceborne GNSS-R receivers can provide global coverage and full temporal availability, and generate simultaneous observations of the Earth's surface along multiple tracks within a wide area.

Future GNSS-R satellite missions will generate an unprecedented level of spatial and temporal coverage (Carreno-Luengo et al., 2021; Winkelried et al., 2023). It is expected that the number of GNSS-R missions, including constellations, will keep increasing in the near future. GNSS-R is a good example of success within the so-called New Space Era, thanks to the improved capabilities of SmallSats platforms, and the long-term plan for deployment and maintenance of GNSS systems (USA GPS, Russian GLObal'naya NAvigatsionnaya Sputnikovaya Sistema or GLONASS, European Galileo, Chinese BeiDou). The significant improvement in coverage will enable improved understanding of Earth's surface dynamic processes.

At present, tracking water bodies remains a challenge for traditional remote sensing satellites because of the limited surface extent of these targets. Multi-spectral VisIR imagers aboard satellites such as Landsat (Pickensa et al., 2020) and Sentinel-2 (Vanderhoof et al., 2023) can generate high-resolution images, but they are affected by issues such as the similarity of spectral water and shadows index, reduced water index of small bodies because of the impact of land contamination, state of surface water etc. Moreover, optical data are limited by night, clouds and intervening biomass cover. On the other hand, C-band Synthetic Aperture Radar (SAR) images by Sentinel-1 in interferometric wide

* Corresponding author.
E-mail address: carreno@umich.edu (H. Carreno-Luengo).

https://doi.org/10.1016/j.rse.2023.113896
Received 28 June 2023; Received in revised form 19 October 2023; Accepted 2 November 2023

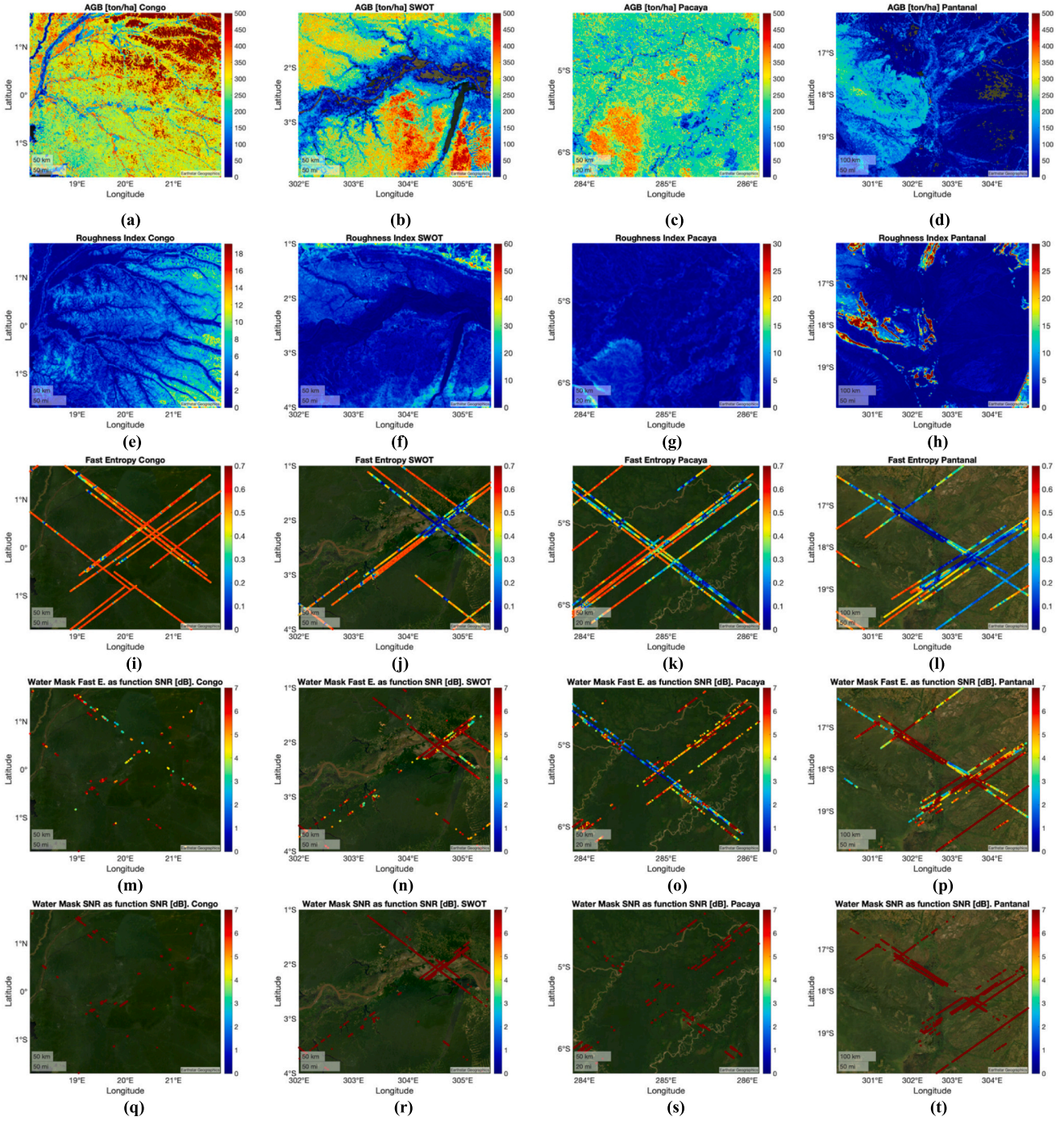

Fig. 1. Above Ground Biomass AGB (a-d), roughness index (e-h), fast entropy coherence detector E_{fast} (j-l), E_{fast} based water masks (m-p), and Signal-to-Noise Ratio *SNR* based water masks (q-t) over: Congo basin (first column), Amazon basin (second column), Pacaya-Samiria region (thirth column), and Pantanal (forth column). Water masks are depicted as a funtion of the *SNR*. E_{fast} detects small water bodies under dense biomass. These results generate better resolution of land-water transitions under dense vegetation, as well as wetland surface extent.

Fig. 2. Scenario over the selected target areas: (a) Amazon rainforests, and (b) Pantanal wetlands. The incident GPS signals are coherently reflected back to space in a bistatic radar configuration, where they are collected by the 8-microsatellites CYGNSS constellation. The Amazon rainforest is a moist broadleaf tropical rainforest. The Pantanal includes the world's largest tropical wetland area, and the world's largest flooded grassland.

mode (Vanderhoof et al., 2023) can generate high-resolution water masks independently of clouds and night conditions, but the images are also limited by the intervening vegetation because of the use of microwave signals at C-band. Finally, it is noteworthy that both types of sensors have a high revisit period, which limits their ability to resolve short term dynamics.

The main objective of this investigation is to develop a new CYGNSS algorithm for water detection under dense biomass using standard L1 reflected power DDMs because of the much lower raw IF data availability. The main challenge of this research is the lack of signal phase information when working with power DDMs. Reflected phase information can be used (Zhang et al., 2022) to accurately classify the surface type between inland water and land, however it can only be extracted with CYGNSS from raw IF data or complex DDMs. The expected relevance of this investigation is high because we aim to improve upon multi-spectral and SAR products by detecting small water bodies under vegetated areas such as tropical rainforests and wetlands, and by developing a significantly improved capability for dynamic monitoring of water extent on the Earth's surface.

A surface water map data product is produced which can be used to further understand the water cycle in tropical latitudes (Pickens et al., 2022) and to better resolve CH4 emission into the atmosphere by tropical wetlands (Parkera et al., 2018). CH4 is a major greenhouse gas that contributes to global warming. Around 30% of total CH4 emission into the atmosphere is generated by wetlands (Ciais et al., 2013). At present, it is speculated that the inter-annual variability of global CH4 is dominated by wetlands, but this is still a matter of investigation in the community (Bousquet et al., 2006). More accurate CH4 emission models require improved capabilities for surface water extent monitoring by remote sensing sensors under dense vegetation.

This manuscript is organized as follows. First, in Section 2 we introduce the scientific observables used. Then, the research motivation is presented in Section 3. Section 4 provides a description of the surface water reference, the algorithm design, and the results over selected target areas in tropical regions. Finally, Section 5 concludes this article.

2. Signal strength observables and coherence detectors

This investigation is focused on generating surface water masks from CYGNSS Level 1 (L1) engineering data. Raw IF data are used to detect signal coherence. In the process, several L1 and raw IF based observables are generated and applied. This Section describes the procedures and

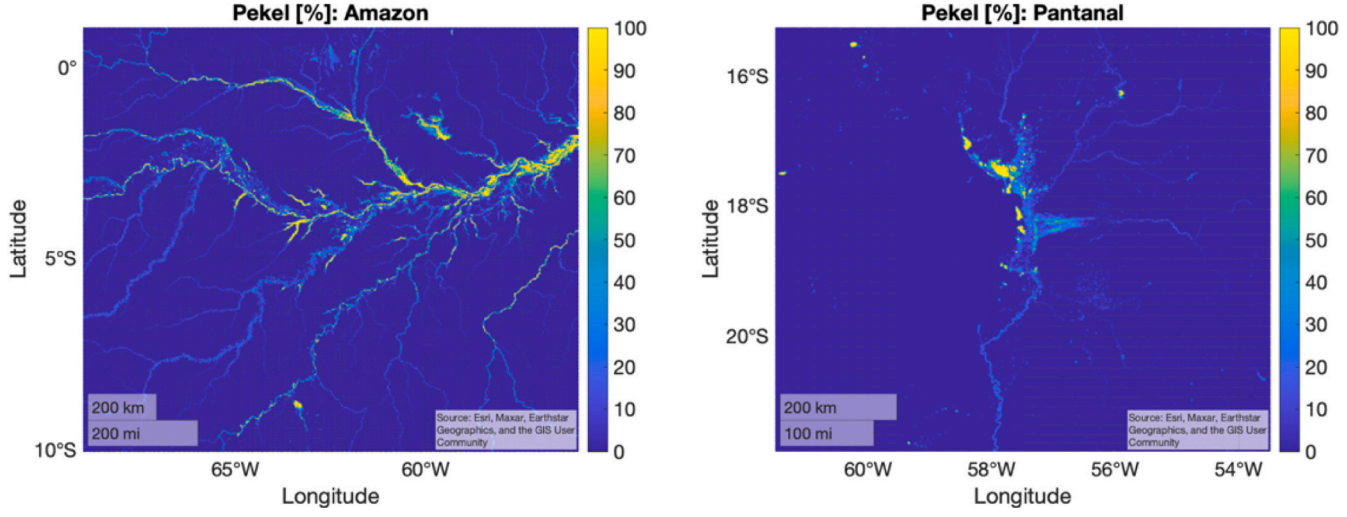

Fig. 3. Pekel surface water occurrence maps over a 0.01° x 0.01° grid: (a) Amazon basin, and (b): Pantanal wetland. This layer represents the percentage of time that water is observed in each cell.

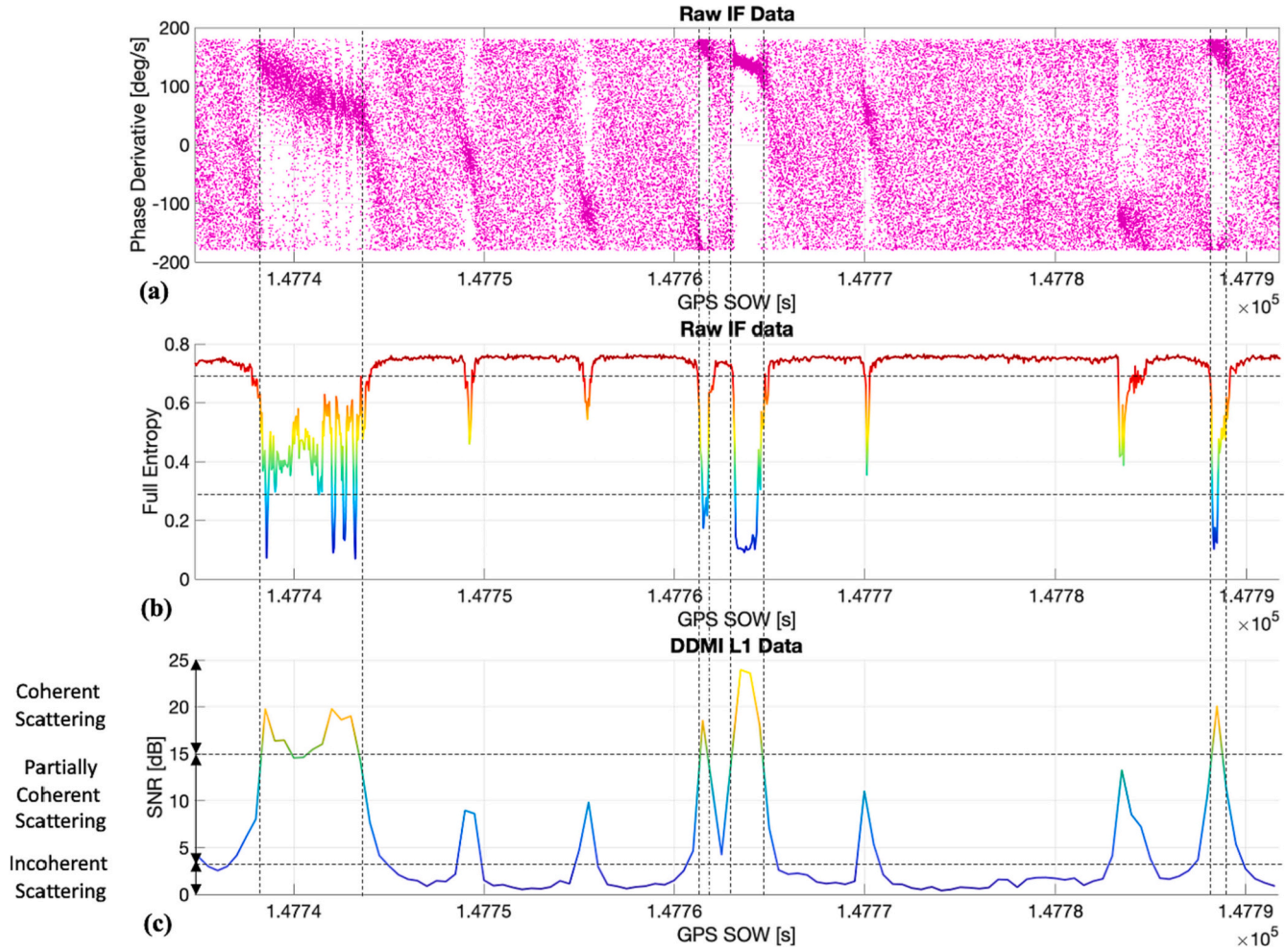

Fig. 4. Time series analysis in a SWOT cal/val site (track acquired on 7 July 2022): (a) derivative of the reflected signal phase φ_{peak}, (b) full entropy coherence detector E_{full}, and (c) L1 Signal-to-Noise Ratio *SNR*. *SNR* levels are used for classification into several GNSS-R scattering regimes, using L1 data generated by the on-board CYGNSS Delay Doppler Mapping Instrument (DDMI): Coherent scattering ($SNR \geq 15$ dB), partially coherent scattering (3 dB $< SNR <$ 15 dB), and incoherent scattering ($SNR \leq 3$ dB).

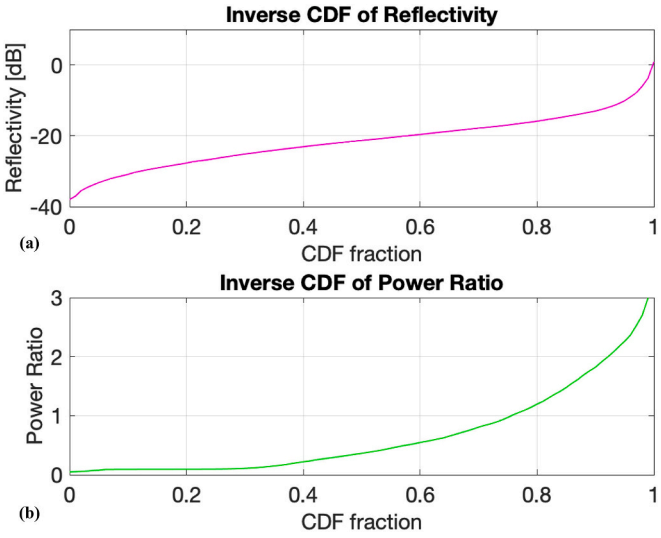

Fig. 5. Inverse Cumulative Distribution Functions (CDFs) of: (a) peak reflectivity Γ_p and (b) power ratio P_{ratio} over land surfaces. 1 month of CYGNSS data is selected over latitudes Lat $= [-40°, 40°]$.

Table 1
2-D Boolean table used to combine two Receiver Operating Characteristic (ROC) curves of peak reflectivity Γ_p and power ratio P_{ratio} using a common inverse Cumulative Distribution Function (CDF) parameterization. For each CDF fraction (Fig. 5), there are two values ($\Gamma_{p,c}$ and $P_{ratio,c}$) that can be used to classify the data (Γ_p and P_{ratio}) in two types (incoherent and coherent scattering), as indicated in the table.

	$\Gamma_p(i) \leq \Gamma_{p,c}$	$\Gamma_p(i) > \Gamma_{p,c}$
$P_{ratio}(i) \leq P_{ratio,c}$	Incoherent	Incoherent
$P_{ratio}(i) > P_{ratio,c}$	Incoherent	Coherent

algorithms used to generate the required signal strength observables and coherence detectors.

2.1. L1 CYGNSS

The Signal-to-Noise Ratio *SNR* is defined as

$$SNR = 10log10\left(\frac{C_p}{C_N}\right) \quad (1)$$

where C_p is the peak of the compressed 17×11 DDMs in raw counts, and C_N is the noise power. Noise information is calculated separately for each DDM, using pixels where no signal power is present i.e. the 45 top

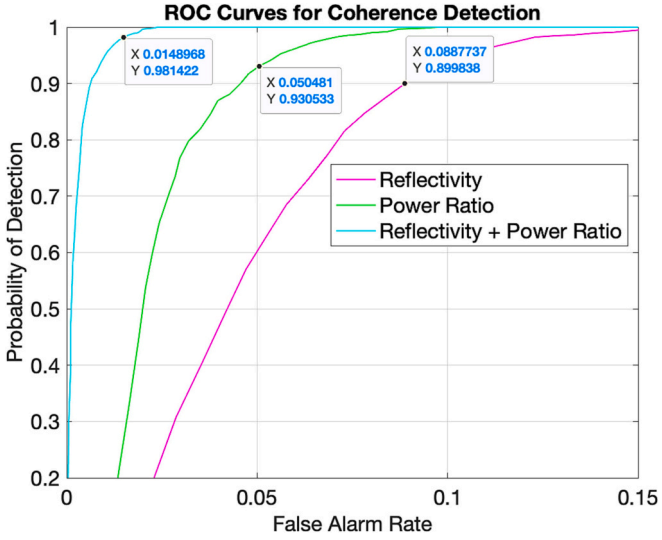

Fig. 6. 1-D ROC curves of peak reflectivity Γ_p and power ratio P_{ratio} and the 2-D ROC curve obtained through the combined use of both observables (Γ_p and P_{ratio}) via a common Inverse Cumulative Distribution Functions (CDFs) parametrization.

delay rows of the original uncompressed 128 × 20 L1 DDMs [$\Delta f = 500$ Hz, $\Delta\tau = 1/4$ chip] or the 180 top delay rows of the 512 × 200 raw IF enhanced resolution DDMs [$\Delta f = 50$ Hz, $\Delta\tau = 1/16$ chip].

The peak reflectivity Γ_p is estimated as (Carreno-Luengo et al., 2015)

$$\Gamma_p = \frac{(4\pi)^2 P_g(\tau_p, f_p)\left(R_r(\tau_p, f_p) + R_t(\tau_p, f_p)\right)^2}{\lambda^2 G_r(\tau_p, f_p) EIRP(\tau_p, f_p)} \tag{2}$$

where P_g is the reflected power after radiometric calibration, R_t and R_r are the ranges from the transmitter and the receiver to the Earth's surface scattering area, λ is the signal electromagnetic wavelength, G_r is the receiver antenna gain, $EIRP$ is the transmitter Equivalent Isotropically Radiated Power, and τ_p and f_p are the peak delay bin and peak Doppler bin of the power DDMs, respectively.

The power ratio P_{ratio} is the ratio of the raw counts of the 3 × 5 delay-Doppler grid surrounding the peak value (compressed 17 × 11 DDMs) over the sum of the rest of the values (Al-Khaldi et al., 2021)

$$P_{ratio} = \frac{P_{ratio,in}}{P_{ratio,out}} \tag{3}$$

where

$$P_{ratio,in} = \sum_{i=-1}^{1}\sum_{j=-2}^{2} C(\tau_p + i, f_p + j) \tag{4}$$

and

$$P_{ratio,out} = \sum_{i=1}^{17}\sum_{j=1}^{11} C(i,j) - P_{ratio,in} \tag{5}$$

2.2. Raw IF CYGNSS

The full entropy detector E_{full} is obtained by applying the Von Neumann entropy definition to the corresponding GNSS-R density matrix

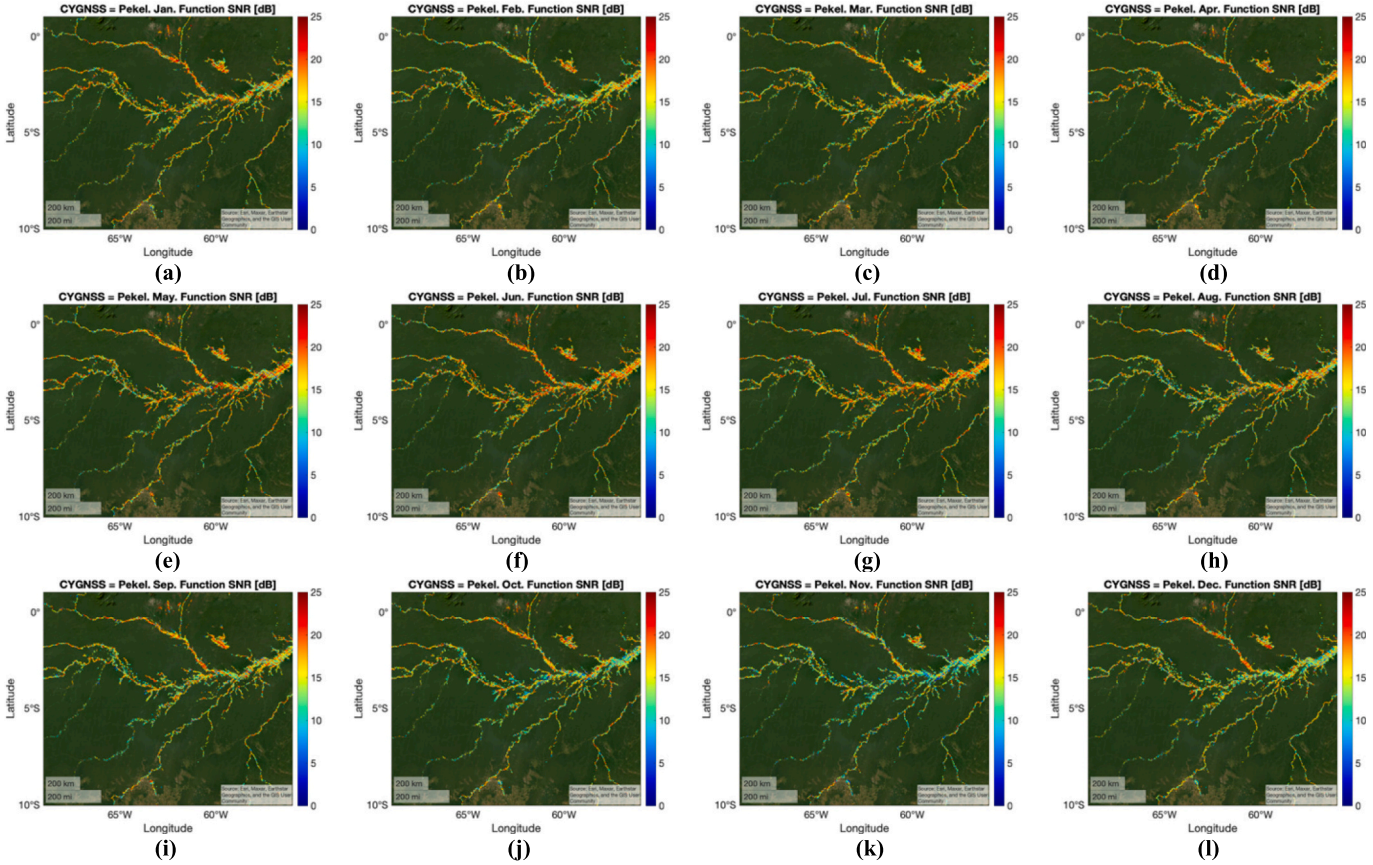

Fig. 7. Amazon basin CYGNSS L1 based monthly water masks over 0.01° x 0.01° grid cells where Pekel also detects water. Maps from January to December 2020 (a-l) are depicted as a function of CYGNSS L1 Signal-to-Noise Ratio *SNR*.

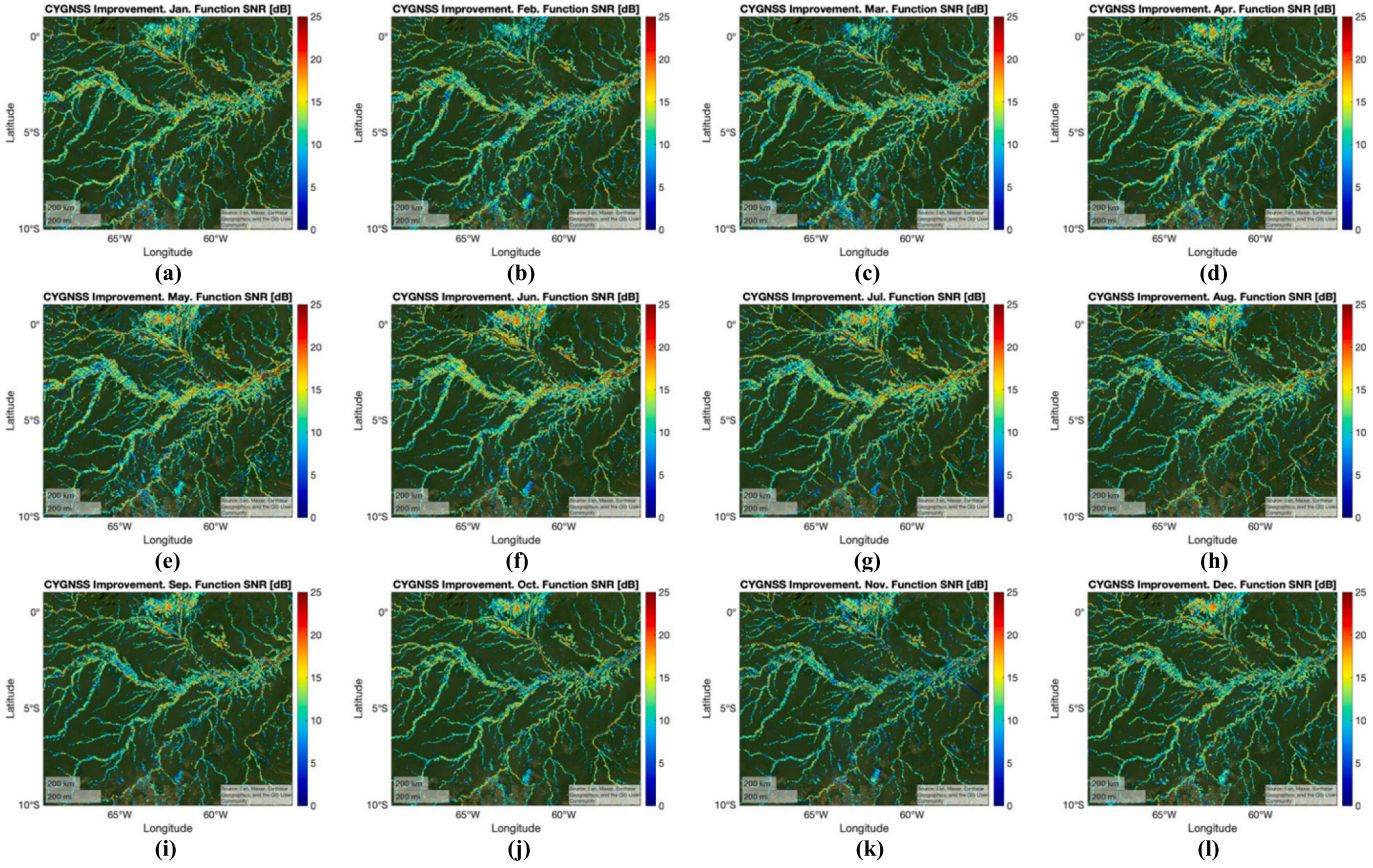

Fig. 8. Amazon basin CYGNSS L1 based monthly water masks over 0.01° x 0.01° grid cells where Pekel does not detect water. Maps from January to December 2020 (a-l) are depicted as a function of CYGNSS L1 Signal-to-Noise Ratio *SNR*.

D_{full}(Russo et al., 2021)

$$E_{full} = -Tr\left(D_{full} log D_{full}\right) \tag{6}$$

where the symbol *Tr* is the trace of the matrix.

The full GNSS-R density matrix D_{Full} is calculated after normalization of the eigenvalues β according to

$$D_{Full} = \frac{\beta}{Tr(\beta)} \tag{7}$$

where β is the diagonal matrix of eigenvalues generated with the Generalized Eigen-Decomposition (GED) of the correlation matrix Q, or

$$\phi^{tp} Q \phi = \beta \tag{8}$$

where ϕ is the matrix of eigenvectors and the superscript *tp* denotes the matrix transpose. Q is generated from sequential snapshots of the zero-Doppler delay waveforms [coherent integration time $T_c = 1$ ms and incoherent integration time $N_{inc} = 1$ ms]. In this study, 48 bins centered at the maximum peak of the waveforms are used for entropy calculations. $Tr(\beta)$ is equal to the sum of its eigenvalues.

Entropy is used as an estimator of the information available in the eigenvalues of the correlation matrix. The eigenvalues are a reliable estimator of the energy distributed along dimensions of the signal subspace. $E_{full} = 1$ represents a uniform eigenvalue distribution, which is an indication of fully incoherent scattering. On the other hand, $E_{full} = 0$ indicates the presence of a dominant eigenvalue, which is an indication of fully coherent scattering. The full entropy E_{full} detector is based on the variation in time of the scattered signal, as well as on the shape of the waveforms.

The fast entropy detector E_{fast} is a computationally fast and approximate calculation of E_{full}. It is computed using the Von Neumann entropy definition as follows:

$$E_{fast} = -Tr\left(D_{fast} log D_{fast}\right) \tag{9}$$

where D_{fast} is the fast GNSS-R density matrix, which is defined by

$$D_{Fast} = \frac{\eta}{Tr(\eta)} \tag{10}$$

where η is the diagonal eigenvalues matrix. η_1 is the largest eigenvalue of the correlation matrix after whitening correlated additive noise Q_w, which is computed using the so-called power method (Andrilli and Hecker, 2010). The second eigenvalue η_2 is defined as the mean value of the remaining eigenvalues. The power method is used to iteratively find the eigenvalue of Q_w that is largest in absolute value i.e. the dominant eigenvalue of Q_w. Although this restriction may seem severe, dominant eigenvalues are of primary interest in many physical applications, which is the case.

Finally, the phase derivative φ_{peak} is also used (Gleason and Gebre-Egziabher, 2009). φ_{peak} is used because it is a well-stablished and reliable signal coherence reference. It is computed as the arctangent of the product of the complex peak $Y_n\left(\tau_p, f_p\right)$ and the conjugate of the previous complex peak $Y_{n-1}\left(\tau_p, f_p\right)$, with $T_c = 1$ ms.

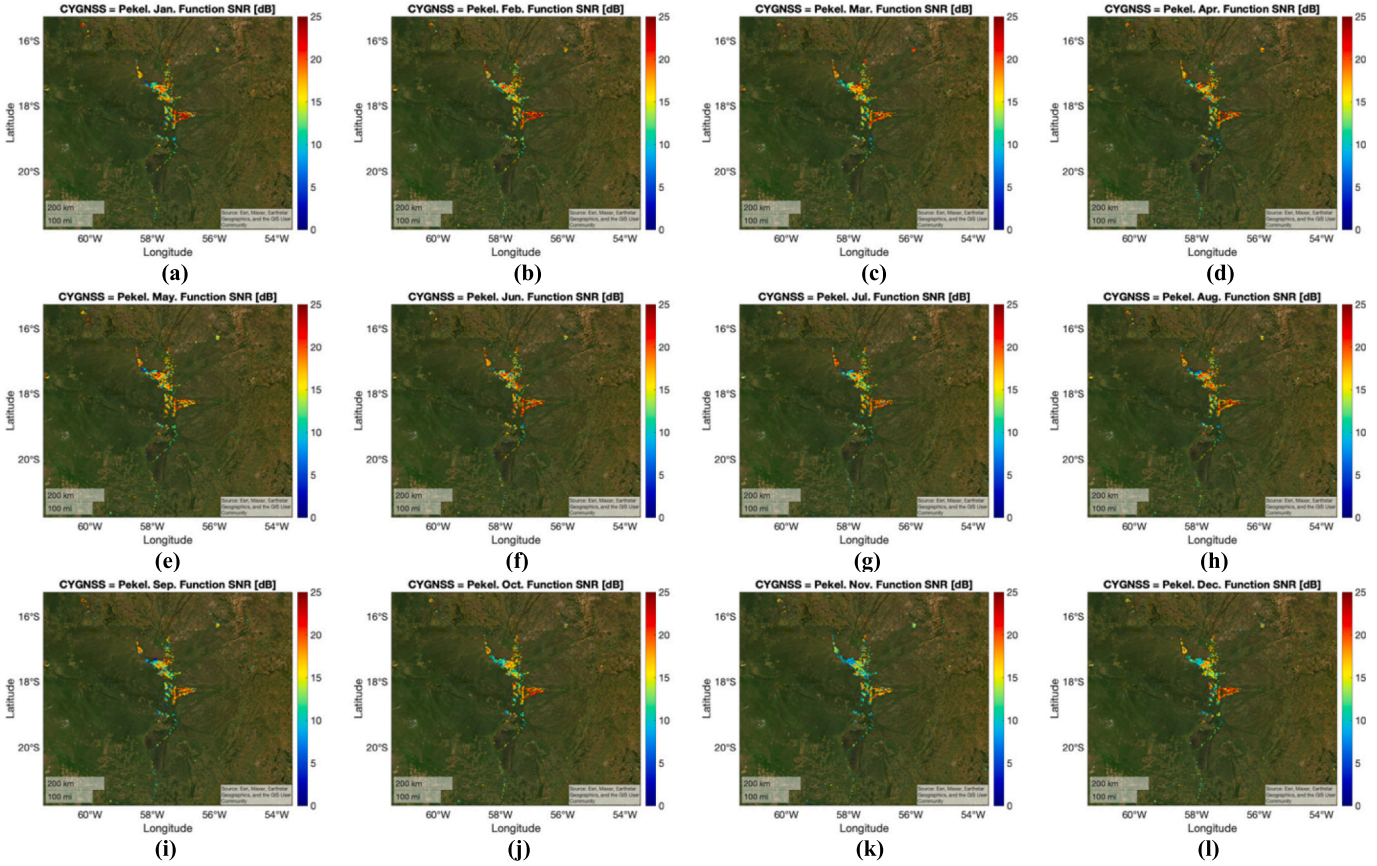

Fig. 9. Pantanal wetlands CYGNSS L1 based monthly water masks over 0.01° x 0.01° grid cells where Pekel detects water. Maps from January to December 2020 (a-l) are depicted as a function of CYGNSS L1 Signal-to-Noise Ratio *SNR*.

3. Research motivation: water detection by raw IF data based observables

During 2022, several CYGNSS raw IF tracks were collected: over the Congo basin; a Surface Water and Ocean Topography (SWOT) cal/val site in the Amazon basin; the Pacaya-Samiria region; and the Pantanal wetlands to evaluate the capability of E_{fast} and *SNR* as coherence detectors for inland water bodies detection under dense biomass (Fig. 1). The temporal resolution of both observables is set to 50 ms. The pantropical Above-Ground Biomass (AGB) dataset by Avitabile et al. (2016) is used as the biomass reference (Fig. 1a-d). AGB levels are high over Congo, Amazon, and Pacaya, and moderate over the Pantanal wetlands. Additionally, a topographic roughness index is included in our study, which is derived from the Amatulli et al. (2018) 250 m resolution digital elevation model, using the method described in (Carreno-Luengo et al., 2019). Maps show that the surface is overall relatively flat over the four selected target areas (Fig. 1e-h).

E_{fast} shows a significant dynamic range, from values up 0.7 when the scattering is incoherent, down to 0.1 when the scattering is highly coherent (Fig. 1i-l). The behavior of E_{fast} as a coherence detector is examined using E_{full} as the reference. The lower computational requirement of E_{fast} as compared to E_{full} makes it suitable for in-orbit water monitoring, and thus it is selected here for evaluation. Performance is characterized using a Receiver Operating Characteristic (ROC) curve. The threshold value corresponding to the optimum operating point of the curve (at which its slope transitions from above to below unity) is used for water detection. A similar methodology is used for the *SNR*. Water masks using $E_{fast} > 0.37$ and $SNR > 7.2$ dB are depicted as a function of the corresponding *SNR* values. This demonstrates that E_{fast} can detect surface water even with quite low *SNR* values (Fig. 1m-p). A physical interpretation is that the reflected signal is coherently scattered over the surface water, but is attenuated by the intervening biomass, with AGB up to 400 ton/ha, and thus the signal strength is low while the signal coherence is preserved. Over the Congo and the Amazon basin, E_{fast} provides improved water detection mainly at land-water transitions, while over the Pacaya-Samiria region and the Pantanal wetlands the improvement is more general because these areas are characterized by extended swamped terrain covered by little vegetation.

Since the amplitude of the coherent signal is generally much higher than the incoherent case, very small water bodies can be detected. In other words, the spatial resolution is directly related to the reflected signal power level. The larger the surface extent of a water body, the larger the reflected power level, when the coherent reflector is smaller than the signal footprint (Camps, 2019). The raw IF based water masks enable these high-interest findings, but since raw IF data availability is reduced, only use of the standard L1 CYGNSS mission data has the potential to study Earth's surface water dynamics with high spatio-temporal sampling. The following questions are addressed in the next Section (Fig. 2): a) Can we define a L1 coherence reference state?; b) What L1 observable provides the best performance for water detection?; and c) What combination of L1 detectors can improve water detection capabilities?

4. Water detection using standard L1 mission data

4.1. Surface water reference: Pekel

The Pekel surface water mask is selected as the main geophysical reference for determination of surface water (Pekel et al., 2016). It is made publicly available by the European Commission (2020). This

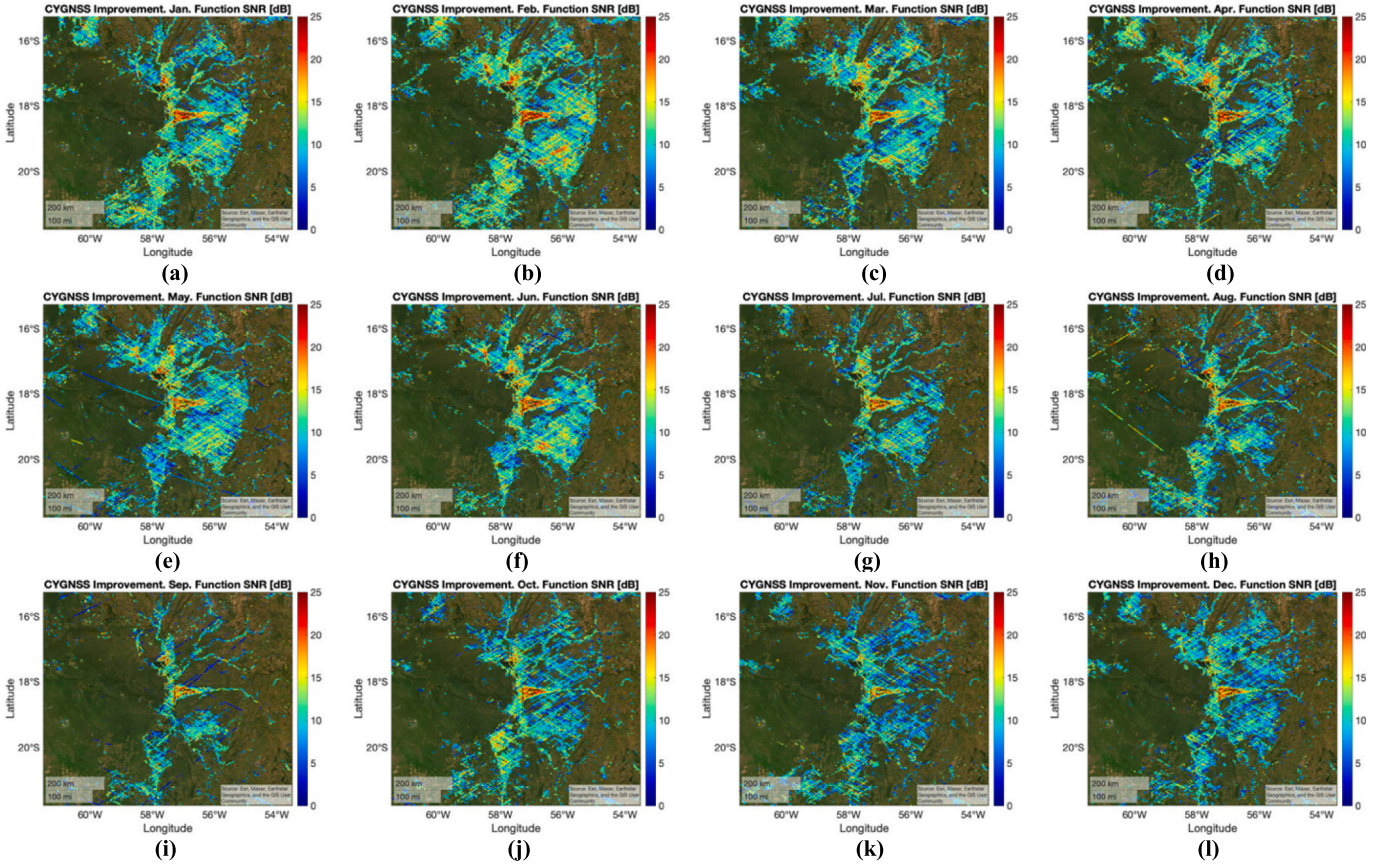

Fig. 10. Pantanal wetlands CYGNSS L1 based monthly water masks over 0.01° x 0.01° grid cells where Pekel does not detect water. Maps from January to December 2020 (a-l) are depicted as a function of CYGNSS L1 Signal-to-Noise Ratio *SNR*.

dataset is built from 37 years of Landsat satellite optical imagery with 30 m spatial resolution. This product is more appropriate for this study than directly using monthly Landsat data because the long revisit period of Landsat satellites. In this work, a re-gridding to 0.01° x 0.01° along with a moving-averaging filter of 0.02° × 0.02° is applied at steps of 0.01° to be compatible with CYGNSS L1 data (Zavorotny et al., 2014).

Fig. 3 shows the surface water occurrence layer obtained using this multi-decade dataset over the Amazon basin (Fig. 3a) and the Pantanal wetlands (Fig. 3b). This layer represents the percentage of time that water is observed in each cell. It can be said that a permanent flooded cell and a permanent land cell correspond to 100% and 0% of occurrence, respectively. Different thresholds can be found in the recent literature for surface water classification (Pickensa et al., 2020; Dettmering et al., 2020; Olthof and Rainville, 2022), however, at the moment, there is not a general consensus in the community. In this work, we identify a cell as water if the Pekel occurrence is >30%. This moderate-to-low threshold is selected to evaluate up to what extent CYGNSS can improve surface water detection even in an optimistic scenario, where a large percentage of cells are assumed to be detected as water by Pekel.

4.2. CYGNSS L1 water detection algorithm

The first step in developing the new L1 algorithm is to establish a scattering classification using standard L1 data. Standard L1 files do not contain IF data nor complex DDMs. Observables can be derived from power DDMs, but no signal phase φ_{peak} nor entropy information (E_{full}, E_{fast}) is available. In this study, raw IF derived E_{full} and φ_{peak} time series are collocated with the on-board generated L1 *SNR* time series in order to enable the desired scattering classification (Fig. 4).

E_{full} is the most reliable coherence detector presented in this study (Loria et al., 2023). The phase derivative at the peak of the reflected complex zero-Doppler delay waveforms φ_{peak} is used to obtain the IF based E_{full} and L1 based *SNR* levels that can be used to classify the different scattering regimes. One raw IF track is selected over a SWOT mission cal/val site to demonstrate the details of this procedure. This region is characterized by the presence of surface water covered by dense vegetation i.e. rainforests (Fig. 2). Underlying water bodies are unresolved by optical sensors e.g. Landsat, and thus this is an interesting scene to be studied. Three different scattering regimes are shown in Fig. 4: a) Coherent scattering ($SNR > 15$ dB), b) partially coherent scattering (3 dB $\leq SNR \leq$ 15 dB), and c) incoherent scattering ($SNR > 3$ dB). These values were found to be consistent along the CYGNSS raw IF tracks collected during 2022. The incoherent scattering regime is characterized by random phase fluctuations and full entropy levels higher than $E_{full} > 0.7$. The partially coherent regime corresponds to full entropy levels between $E_{full} \geq 0.3$ and $E_{full} \leq 0.7$ and is characterized by a noisy linear trend of the phase derivative φ_{peak}.Finally, the coherent scattering regime is found for full entropy levels below $E_{full} < 0.3$ and φ_{peak} is clearly resolved in this state. In this scenario, when the surface is smooth, the scattering is highly coherent, and the reflected signal phase can be tracked reliably.

The next step is to evaluate the performance of the available L1 observables as coherent detectors. Reflectivity Γ_p and power ratio P_{ratio} can each be used separately for inland water detection (Al-Khaldi et al., 2021; Chew et al., 2023). The *SNR* is a measure of received signal strength, which scales linearly with the reflectivity Γ_p of the surface. Reflectivity is in turn sensitive to both the surface permittivity and roughness. The power ratio P_{ratio}, on the other hand, is an indicator of

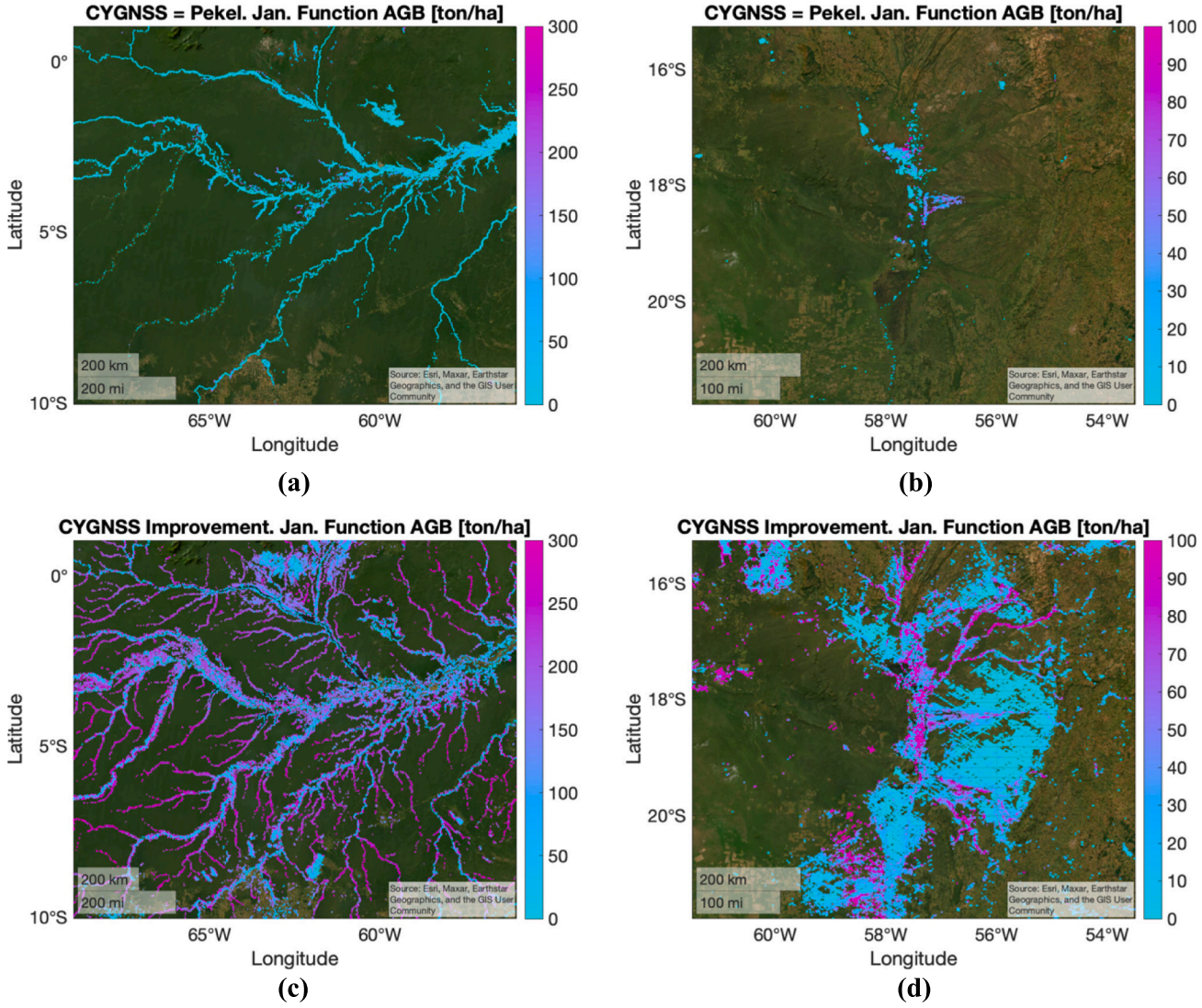

Fig. 11. CYGNSS L1 based monthly water masks over 0.01° x 0.01° grid cells where the Pekel detects water (a,b) and over 0.01° x 0.01° grid cells where Pekel does not detect water (c,d). Maps are depicted as a function of Above Ground Biomass AGB (Avitabile et al., 2016) for: (a,c) Amazon basin, and (b,d) Pantanal wetlands. CYGNSS L1 water masks are able to detect water under dense biomass, providing a significant improvement as compared to water masks dervied from state-of-the art Landsat optical data (Pekel et al., 2016).

the spread of the scattering of the GPS signal over the Earth's surface due to diffuse (i.e. incoherent) scattering and is primarily sensitive to surface roughness alone. If the surface is flat, the power ratio P_{ratio} is high, and it gradually decreases as the surface roughness increases. The reflectivity Γ_p is high when the surface permittivity is high or when the surface roughness is low, and it will gradually decrease as either the permittivity decreases or the roughness increases. Reflectivity is also affected by vegetation, with a denser, more attenuating vegetation canopy producing a lower reflectivity. These differences in their sensitivity to surface conditions are exploited by the combined P_{ratio} and Γ_p detection algorithm.

Both detectors are here combined in a joint detection algorithm with improved capabilities over either one alone for water monitoring. A 2-D Boolean algorithm is used to combine 2 ROC curves (for Γ_p and P_{ratio}) using a common inverse Cumulative Distribution Function (CDF) parameterization. For each CDF fraction (Fig. 5), there are two values ($\Gamma_{p,c}$ and $P_{ratio,c}$) that can be used to classify the data (Γ_p and P_{ratio}) in two types (incoherent and coherent scattering), as indicated in Table 1. This information is used to compute the ROC curves (Fig. 6), which show the capability of diagnosis of a binary classifier as a function of the selected system threshold. ROC curves are computed using the previous scattering classification as proxy data: The scattering is considered fully incoherent if $SNR < 3$ dB, and fully coherent when $SNR > 15$ dB. The performance of the 2-D ROC curve increases the Probability of Detection (PD) and reduces the False Alarm Rate (FAR) as compared to the 1-D ROC curves using P_{ratio} or Γ_p individually. This improvement is obtained because this combination method leverages more information contained in the reflected DDMs than the individual observables do. For example, in scenarios where Γ_p is low, adding P_{ratio} data is helpful to elucidate what type of scattering is dominant. The thresholds $\Gamma_p >$ -17.706 dB and $P_{ratio} > 0.805$ corresponding to the optimum point of the 2-D ROC curve are hereafter used for water detection. The optimum operating point of a ROC curve, at which the slope of the curve crosses from above to below unity, marks the transition from more true than false detections to more false than true. The ROC curves are based on 3 months of GNSS-R data over land surfaces, including a wide variety of land cover types within the CYGNSS coverage, and they are independent of external parameters.

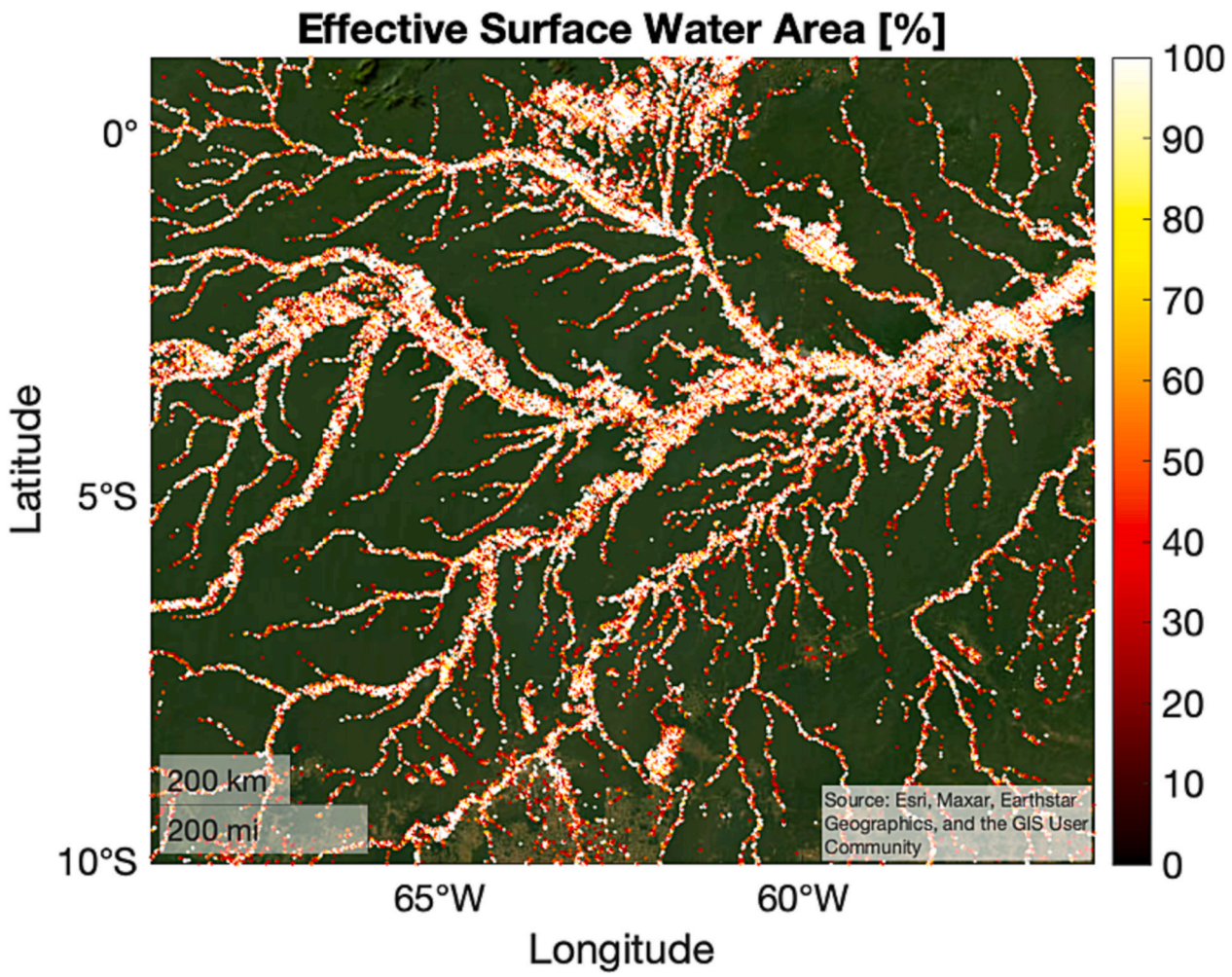

Fig. 12. Effective surface water area per grid cell over the Amazon basin during January 2020. This parameter appears lower in cells with small water bodies and in cells located at the borders of water bodies. The surface water extent within this type of cells is lower than over cells centered on extended flooded terrain.

4.3. *CYGNSS L1 water masks: impact on methane emission*

The new CYGNSS L1 water detection algorithm based on the 2-D ROC curve is now applied to the full 2020 CYGNSS L1 v3.0 dataset (500 ms incoherent integration time). L1 data are averaged spatially and temporally in monthly periods. Then, the surface water maps are generated using the thresholds previously described ($\Gamma_p >$ -17.706 dB and $P_{ratio} > 0.805$). This study covers both the rainy and the dry seasons over the two selected target areas: the Amazon basin, which is the world's largest remaining tropical rainforest; and the Pantanal (Fig. 2), which is the world's largest tropical wetland. Most of the Earth's wetlands are in tropical latitudes, and thus the tropical latitude band covered by CYGNSS Lat. $= [-40°, 40°]$ is of high interest for scientists investigating the impact of wetland extent on methane CH4 emissions to the atmosphere. In the tropics there are pronounced precipitation changes throughout the year, which influence the seasonal variability of CH4 emission. Uncertainties in surface water extent in maps currently produced by optical and SAR instruments aboard satellites generate errors in modeled CH4 emissions. Masks produced by these instruments can be severely affected by vegetation. Currently, there are no remote sensing instruments capable of generating water masks under dense biomass.

CYGNSS L1 based monthly water maps are depicted as a function of *SNR* (color represents *SNR*) over the Amazon basin (Figs. 7,8) and Pantanal wetlands (Figs. 9,10). Figs. 7 and 9 show grid cells where both CYGNSS ($\Gamma_p >$ -17.706 dB and $P_{ratio} > 0.805$) and Pekel (Pekel occurrence $>$ 30%) detect water. Figs. 8 and 10 show grid cells where CYGNSS detects water, but Pekel does not (Pekel occurrence $\leq$ 30%), likely due to the presence of significant vegetation. There is a remarkable difference between both type of maps. The *SNR* levels are very strong up to 20 dB in grid cells where Pekel detects water, while *SNR* is significantly lower down to 5 dB in cells where Pekel does not detect water because of the vegetation cover. The water detection improvement by this new CYGNSS L1 algorithm is significant, showing the capability of water monitoring even with low *SNR* values. This enables, for example, the detection of small rivers over complex heterogeneous scenes including both tropical rainforests and wetlands.

The relevance of these findings is high because these improved water masks can be used by CH4 emission models to better quantify emission into the atmosphere (e.g. Eq. (1) in Bloom et al., 2017). Additionally, thanks to its high spatial-temporal sampling, CYGNSS can generate water masks much more frequently than current state-of-the art techniques such as optical or SAR missions. The objective of this work is the presentation of the algorithm and the improvement over vegetated areas as compared to Pekel. The use of all L1 data generated by future GNSS-R missions will generate an unprecedented amount of power DDMs, enabling the monitoring of highly dynamic inland water bodies processes with higher frequency and spatial resolution. In the case of GNSS-

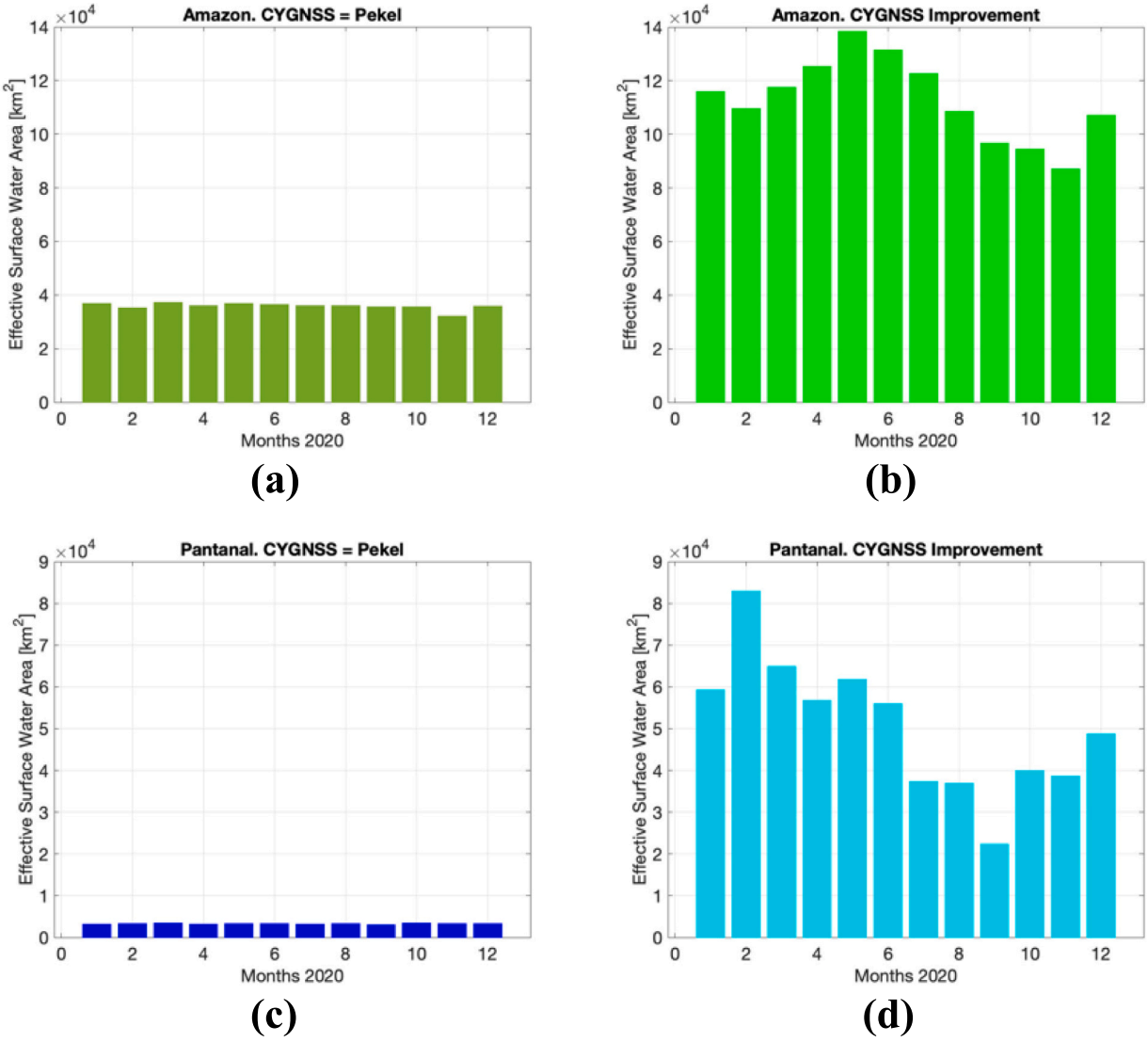

Fig. 13. Effective monthly surface water area during 2020 over: (a,b) Amazon basin, and (c,d) Pantanal wetlands. Data are depicted in: (a,c) regions where CYGNSS and Pekel agree about detected water, and (b,d) regions where CYGNSS improves upon Pekel.

R measurements, a larger number of measurements over a target area allows for a reduction in the cell size used in the generation of the maps. In so doing, the application of a standard procedure by the scientific community (Carreno-Luengo et al., 2021) is key for the generation of a virtual GNSS-R satellites constellation or constellation of constellations (Ruf et al., 2023; Jales et al., 2020; Masters et al., 2023; Unwin et al., 2021). This system will overcome the performance limitations of optical and SAR missions.

4.4. CYGNSS L1 water masks: evaluation with biomass

CYGNSS maps of surface water extent are evaluated as a function of AGB (Avitabile et al., 2016), which is one relevant geophysical parameter that attenuates the transmitted GPS signals along its propagation path through the vegetation cover (Santi et al., 2020). CYGNSS maps agree with Pekel optical Landsat data in areas with negligible AGB (Fig. 11a,b). On the other hand (Fig. 11c,d), the new CYGNSS L1 water detection algorithm can detect small water bodies under thick biomass up to 400 ton/ha over the Amazon basin (Fig. 11c).

The scattered GPS signals as collected by CYGNSS are coherently scattered over surface water when the Rayleigh criterion for a surface to be considered smooth is satisfied (Carreno-Luengo et al., 2014)

$$\sigma < \frac{\lambda}{8 sin\theta_e} \tag{11}$$

where σ means surface height standard deviation, θ_e is the elevation angle, and λ is GPS L1 wavelength 19 cm. In other words, the surface water can be considered smooth when the phase difference between all the scatterers is lower than $\pi/2$. In practice, this translates to coherent signal returns when $\sigma = [2, 4]$ cm, for the selected range $\theta_e = [40°, 90°]$.

The coherently scattered GPS signals are attenuated by the intervening vegetation cover. Consequently, the *SNR* decreases in regions with significant biomass (Fig. 11). It is worth highlighting that over the Pantanal wetlands, CYGNSS can resolve surface water extent, while Pekel fails. The Pantanal is characterized by low-to-moderate AGB, but this thin biomass cover is nonetheless sufficient to significantly limit the performance of optical data for water body detection, i.e. Pekel.

After scattering and propagation, the coherent scattering term $\left\langle |Y_{coh}|^2 \right\rangle$ can be modeled as follows (Carreno-Luengo et al., 2015; Camps et al., 2016)

$$\left\langle |Y_{coh}|^2 \right\rangle = \frac{\lambda^2 EIRP G_r |\chi|^2}{(4\pi)^2 (R_r + R_t)^2} |R_{r,l}(\theta_e)|^2 e^{-2VOD/sin\theta_e} e^{-(2k\sigma sin\theta_e)^2} \tag{12}$$

where χ is the so-called Woodward Ambiguity Function, $R_{r,l}$ is the cross-pol Fresnel reflection coefficient, the subscripts r and l denote right- and left- hand circular polarization, *VOD* is the vegetation optical depth, and k is the signal angular wavenumber. $R_{r,l}$ can be assumed to be roughly constant in the selected range $\theta_e = [40^\circ, 90^\circ]$. *VOD* is a parameter that characterizes the attenuation of microwave signals through vegetation as a function of vegetation water content and vegetation structure.

Since path losses are inversely proportional to $(R_r + R_t)^2$, where $R_r \ll R_t$, $\left\langle |Y_{coh}|^2 \right\rangle$ is less attenuated than the incoherent scattering term $\left\langle |Y_{incoh}|^2 \right\rangle$ (Zavorotny et al., 2014), which is inversely proportional to $(R_r R_t)^2$. This is the analytical justification of the strong *SNR* of the GPS signals after reflection over water surface, despite the impact of attenuation by the vegetation cover through the term $e^{-2VOD/\sin\theta_e}$ (Camps et al., 2016; Santi et al., 2020). At lower θ_e, signal attenuation is larger, but signal coherence increases, following the Rayleigh criterion. Empirical results show that the effective surface roughness is lower than theoretical predictions (Carreno-Luengo and Camps, 2015). This effect explains why most CYGNSS observations over surface water bodies are coherent. In the Pantanal wetlands the *SNR* levels are relatively low (Fig. 10) despite the fact that biomass density is low-to-moderate (Fig. 11d). The physical explanation of this observation is that the higher surface roughness σ of large extended wetlands as compared to small water bodies such as rivers reduces signal coherence, but the effective roughness is still low enough to support coherent reflections.

4.5. CYGNSS L1 water masks: effective surface water area

The effective surface water area per grid cell is here defined as the percentage of water detection cases with respect to the total number of measurements in each cell. This parameter is lower in cells with small water bodies and in cells located on the border of water bodies (Fig. 12). The surface water extent within this type of cells is lower than for cells centered in more extended flooded terrain. This explains the increment of the effective area in regions with larger surface water bodies (Fig. 12). The temporal evolution of water extent covers both the rainy and dry seasons over the two selected target areas during 2020. This evaluation is performed in regions where CYGNSS and Pekel agree, and in regions where CYGNSS improves upon the performance of the Pekel surface water mask (Fig. 13). In the first case, the temporal evolution is roughly constant, while in the former scenario the area presents significant fluctuations, which agree with the annual dry and rainy seasons in the Amazon basin (dry from July to November and rainy from December to June) (Li and Min, 2013) and the Pantanal wetlands (dry from May to September and rainy from October to April) (Evans et al., 2014). These results illustrate the capability of CYGNSS to aid in our further understanding of the temporal dynamics of Earth's surface water.

Appendix A. Local case study over the Amazon basin

5. Conclusion

A new CYGNSS surface water detection algorithm based on standard L1 mission power DDMs has been developed and applied over the Amazon basin and the Pantanal wetlands. The new algorithm is validated using the full entropy coherence detector E_{full} and the derivative of the reflected signal phase φ_{peak} obtained from raw IF data. We find that GPS signals are coherently reflected from surface water bodies despite the impact of the intervening biomass cover. Results show the capability to detect and image small water bodies under heavy vegetation i.e. 400 ton/ha. This CYGNSS improvement as compared to Pekel water mask derived from optical imagers allows for monitoring of the temporal fluctuations of surface water even in densely vegetated areas. We demonstrate that the NASA CYGNSS mission is capable of detecting surface water even with low *SNR* levels. In the future, larger constellations of SmallSats carrying GNSS-R instruments could be used to generate water masks with significantly improved spatio-temporal sampling capabilities. This could revolutionize the monitoring of highly dynamic surface hydrological processes, such as those related to flood inundation and seasonal expansion and contraction of persistent water bodies.

CRediT authorship contribution statement

Hugo Carreno-Luengo: Conceptualization, Methodology, Software, Validation, Formal analysis, Writing – original draft, Writing – review & editing, Visualization. **Christopher S. Ruf:** Conceptualization, Methodology, Writing – review & editing, Project administration, Funding acquisition. **Scott Gleason:** Methodology. **Anthony Russel:** Software.

Declaration of Competing Interest

The authors declare that they have no known competing financial interests or personal relationships that could have appeared to influence the work reported in this paper.

Data availability

Data will be made available on request.

Acknowledgement

This research was supported in part by the NASA Science Mission Directorate contract 80LARC21DA003 with The University of Michigan (UMich).

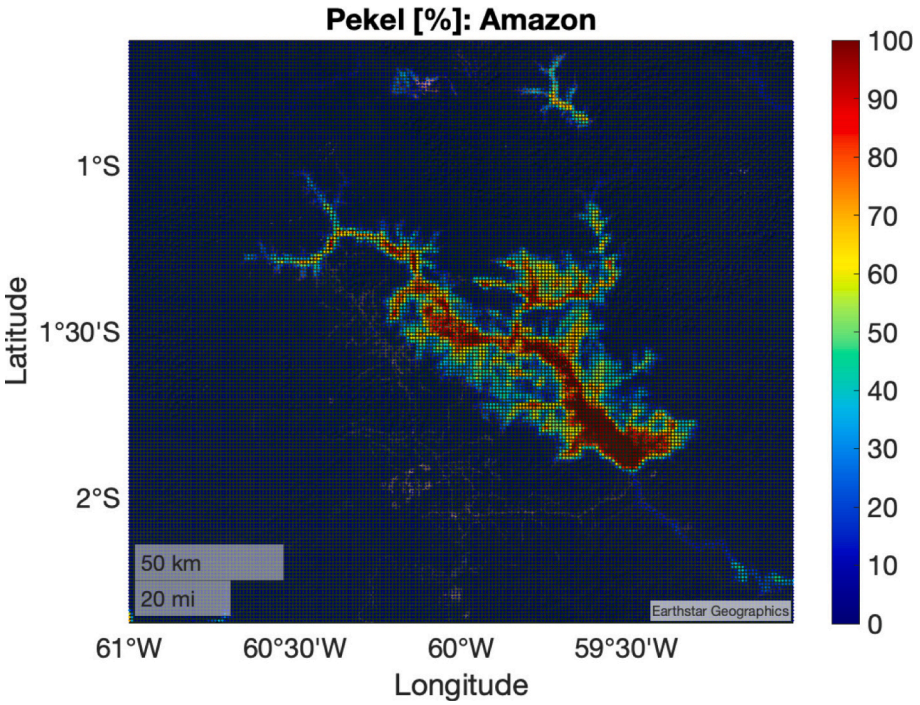

(a)

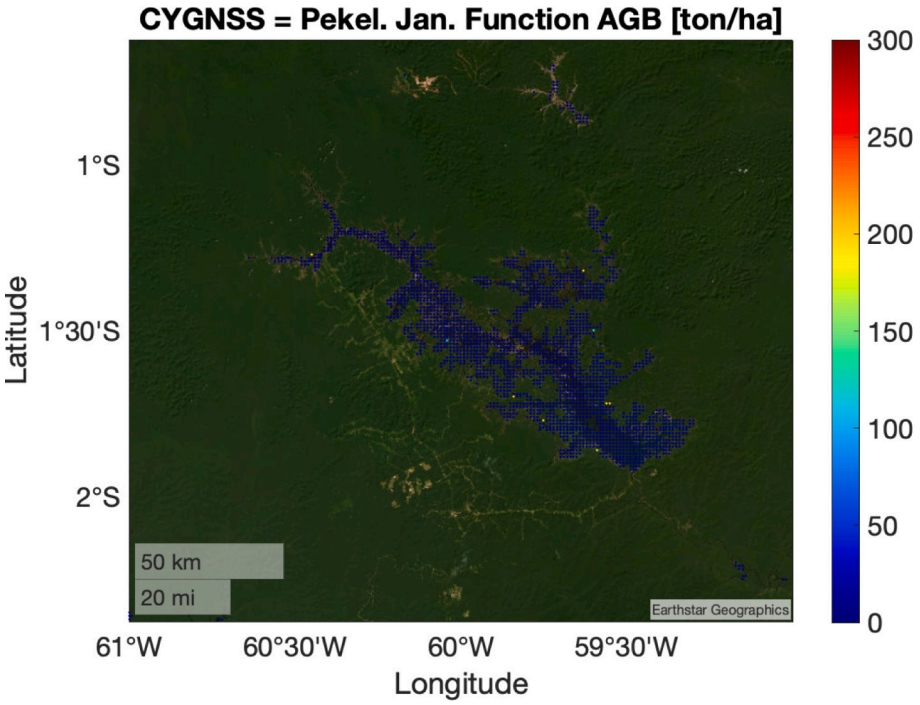

(b)

Fig. 14. Local case study over the Amazon basin: (a) Pekel surface water occurrence map, (b) surface water map where both CYGNSS (2-D Boolean algorithm using Γ_p and P_{ratio}) and Pekel (Pekel occurrence is >30%.) detect water, (c) surface water map where only CYGNSS (2-D Boolean algorithm using Γ_p and P_{ratio}) detects water. This case study over the Amazon basin is included to show the capability of water detection under dense biomass over a local area because the 0.01° x 0.01° grid cells are small. The different type of cells (CYGNSS and Pekel detect water vs. only CYGNSS detect water) are interleaved, but there is not any overlap of the pixels as it is clearly demonstrated in Fig. 14. The surface water occurrence layer represents the percentage of time that water is observed in each cell. The Pekel product is build using 37 years of data, which mitigates the impact of clouds when they are over the area. In Fig. 11 there are two type of maps (CYGNSS and Pekel detect water) and (CYGNSS detect water but Pekel does not). All of these maps are depicted as a function of biomass (Avitabile et al., 2016). It is found that biomass is negligible in regions where Pekel detects water, but biomass is from low to very high in regions where Pekel does not detect water. However, independent of the Pekel capabilities, it is clearly demonstrated that CYGNSS detects water under dense biomass. Finally, we would like to highlight that optical data such as Pekel can only detect open water bodies (or with negligible vegetation). Consequently, the previous classification is intrinsically a way to classify pixels in two classes, open

water (Fig. 14b), and not open water (Fig. 14c). It is also worth to point out that the Pekel surface water detection is affected by the fact that the Pekel occurrence layer represents the percentage of time that water is observed in each cell. On the other hand, the CYGNSS product is more realistic, based on geophysical properties estimated from the scattered GPS signals and validated using raw IF measurements.

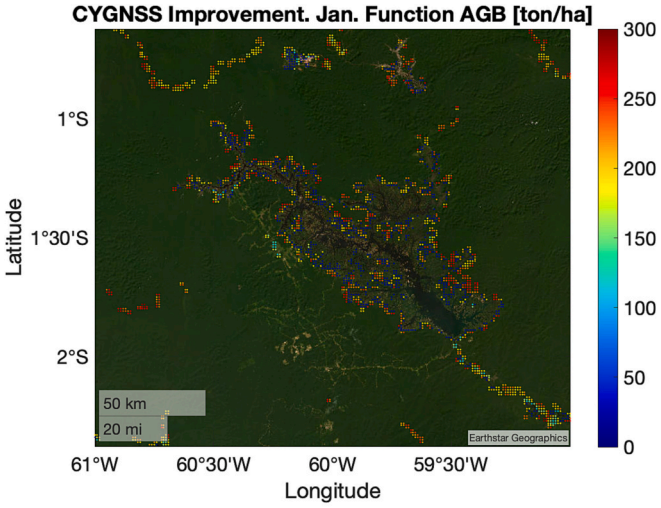

(c)

Fig. 14. (*continued*).

References

Al-Khaldi, M.M., Johnson, J.T., Gleason, S., Chew, C., Gerlein-Safdi, C., Shah, R., Zuffada, C., 2021. Inland water body mapping using CYGNSS coherence detection. IEEE Trans. Geosci. Remote Sens. 59 (9), 7385–7394. https://doi.org/10.1109/TGRS.2020.3047075.

Amatulli, G., Domisch, S., Tuanmu, M.-N., Parmentire, B., Ranipeta, A., Malczyk, J., Jetz, W., 2018. A suite of global cross-scale topographic variables for environmental and biodiversity modelling. Nat. Sci. Data 180040.

Andrilli, S., Hecker, D., 2010. Elementary Linear Algebra. Elsevier, Amsterdam, Netherlands. ISBN: 978–0–12-374751-8.

Avitabile, et al., 2016. An integrated pan-tropical biomass map using multiple reference datasets. Glob. Chang. Biol. 2, 1406–1420. https://doi.org/10.1111/gcb.13139.

Bloom, A., Bowman, K.W., Lee, M., Turner, A.J., Schroeder, R., Worden, J.R., Weidner, R., McDonald, K.C., Jacob, D.J., 2017. A global wetland methane emissions and uncertainty dataset for atmospheric chemical transport models (WetCHARTs version 1.0). Geosci. Model Dev. 10 (6), 2141–2156. https://doi.org/10.5194/gmd-10-2141-2017.

Bousquet, P., Ciais, P., Miller, J.B., Dlugokencky, E.J., Hauglustaine, D.A., Prigent, C., Van Der Werf, G.R., Peylin, P., Brunke, E., Carouge, C., Langenfelds, R.L., Lathiere, J., Papa, F., Ramonet, M., Schmidt, M., Steele, L.P., Tyler, S.C., White, J., 2006. Contribution of anthropogenic and natural sources to atmospheric methane variability. Nature 443 (7110), 439–443. https://doi.org/10.1038/nature05132.

Camps, A., 2019. Spatial resolution in GNSS-R under coherent scattering. IEEE Geosci. Remote Sens. Lett. 17 (1), 32–36. https://doi.org/10.1109/LGRS.2019.2916164.

Camps, A., 2021. Introduction to Remote Sensing Using GNSS Signals of Opportunity, Ocean Remote Sensing Technologies: High Frequency, Marine and GNSS-Based Radar. The Institution of Engineering and Technology, Stevenage, United Kingdom, Book SECTION 18. ISBN-13: 978-1-83953-161-3.

Camps, A., Park, H., Pablos, M., Foti, G., Gommenginger, C.P., Liu, P.W., Judge, J., 2016. Sensitivity of GNSS-R spaceborne observations to soil moisture and vegetation. IEEE J. Sel. Top. Geosci. Remote Sens. 9 (10), 4730–4732. https://doi.org/10.1109/JSTARS.2016.2588467.

Cardellach, E., Wickert, J., Baggen, R., Benito, J., Camps, A., Catarino, N., Chapron, B., Dielacher, A., Fabra, F., Flato, G., Fragner, H., Gabarro, C., Gommenginger, C., Haas, C., Healy, S., Hernandez-Pajares, M., Høeg, P., Jäggi, A., Kainulainen, J., Khan, S.A., Lemke, N., Li, W., Nghiem, S.V., Pierdicca, N., Portabella, M., Rautiainen, K., Rius, A., Sasgen, I., Semmling, M., Shum, C.K., Soulat, F., Steiner, A. K., Tailhades, S., Thomas, M., Vilaseca, R., Zuffada, C., 2018. GNSS transpolar earth reflectometry exploriNg system (G-TERN): mission concept. IEEE Access 6, 13980–14018. https://doi.org/10.1109/ACCESS.2018.2814072.

Carreno-Luengo, H., Camps, A., 2015. Empirical results of a surface level GNSS-R experiment in a wave channel. MDPI Remote Sens. 7 (6), 7471–7493. https://doi.org/10.3390/rs70607471.

Carreno-Luengo, H., Camps, A., Ramos-Pérez, I., Rius, A., 2014. Experimental evaluation of GNSS reflectometry altimetric precision using the P(Y) and C/A signals. IEEE J. Sel. Top. Geosci. Remote Sens. 7 (5), 1493–1500. https://doi.org/10.1109/JSTARS.2014.2320298.

Carreno-Luengo, H., Camps, A., Querol, J., Forte, G., 2015. First results of a GNSS-R experiment from a stratospheric balloon over boreal forests. IEEE Trans. Geosci. Remote Sens. 54 (5), 2652–2663. https://doi.org/10.1109/TGRS.2015.2504242.

Carreno-Luengo, H., Luzi, G., Crosetto, M., 2019. First evaluation of topography on GNSS-R: an empirical study based on a digital elevation model. MDPI Remote Sens. 11 (21), 2556. https://doi.org/10.3390/rs11212556.

Carreno-Luengo, H., Camps, A., Floury, N., Martin-Neira, M., Ruf, C., Wang, T., Khalsa, S. J., Clarizia, M.P., Reynolds, J., Johnson, J., O'Brien, A., Galdi, C., di Bisceglie, M., Dielacher, A., Jales, P., Unwin, M., King, L., Foti, G., Shah, R., Pascual, D., Schreiner, B., Asgarimehr, M., Wickert, J., Ribo, S., Cardellach, E., 2021. IEEE standard for spaceborne global navigation satellite system-reflectometry (GNSS-R) data and metadata content. IEEE Stand. Assoc. https://doi.org/10.1109/IEEESTD.2021.9594781.

Chew, C., Small, E., Huelsing, H., 2023. Flooding and inundation maps using interpolated CYGNSS reflectivity observations. Remote Sens. Environ. 293, 113598 https://doi.org/10.1016/j.rse.2023.113598.

Ciais, P., Sabine, C., Bala, G., Bopp, L., Brovkin, V., Canadell, J., Chhabra, A., DeFries, R., Galloway, J., Heimann, M., Jones, C., Le Quéré, C., Myneni, R., Piao, S., Thornton, P., 2013. Carbon and Other Biogeochemical Cycles. Cambridge University Press, Cambridge, United Kingdom and New York, NY, USA, pp. 465–570. Book Section 6. https://doi.org/10.1017/CBO9781107415324.015.

Dettmering, D., Ellenbeck, L., Scherer, D., Schwatke, C., Niemann, C., 2020. Potential and limitations of satellite altimetry constellations for monitoring surface water storage changes—A case study in the Mississippi basin. MDPI Remote Sens. 12 (20), 3320. https://doi.org/10.3390/rs12203320.

Downs, B., Kettner, A.J., Chapman, B.D., Brakenridge, G.R., O'Brien, A.J., Zuffada, C., 2023. Assessing the relative performance of GNSS-R flood extent observations: case study in South Sudan. IEEE Trans. Geosci. Remote Sens. 61, 4201213. https://doi.org/10.1109/TGRS.2023.3237461.

European Commission, 2020. Global Surface Water Explorer. https://global-surface-water.appspot.com (accessed 25 May 2023).

Evans, T.L., Costa, M., Tomas, W.M., Camilo, A.R., 2014. Large-scale habitat mapping of the Brazilian Pantanal wetland: a synthetic aperture radar approach. Remote Sens. Environ. 155, 89–108. https://doi.org/10.1016/j.rse.2013.08.051.

Garrison, J.L., Katzberg, S.J., 2000. The application of reflected GPS signals to ocean remote sensing. Remote Sens. Environ. 73 (2), 175–187. https://doi.org/10.1016/S0034-4257(00)00092-4.

Gerlein-Safdi, C., Bloom, A.A., Plant, G., Kort, E.A., Ruf, C.S., 2021. Improving representation of tropical wetland methane emissions with CYGNSS inundation maps. AGU Glob. Biogeochem. Cycles 35 (12). https://doi.org/10.1029/2020GB006890 e2020GB006890.

Gleason, S., Gebre-Egziabher, D., 2009. GNSS Applications and Methods. Artech House, Norwood, MA, USA. ISBN: 978–1–59693-329-3.

Jales, P., Esterhuizen, S., Masters, D., Nguyen, V., Nogués Correig, O., Yuasa, T., Cartwright, J., 2020. The new spire GNSS-R satellite missions and products. In: Proc. of the SPIE Image Signal Processing Remote Sensing XXVI, 2020, p. 1153316. https://doi.org/10.1117/12.2574127.

Li, R., Min, Q., 2013. Dynamic response of microwave land surface properties to precipitation in Amazon rainforest. Remote Sens. Environ. 133, 183–192. https://doi.org/10.1016/j.rse.2013.02.001.

Loria, E., Russo, I.M., Wang, Y., Giangregorio, G., Galdi, C., di Bisceglie, M., Wilson-Downs, B., Lavalle, M., O'Brien, A.J., Morton, J., Zuffada, C., 2023. Comparison of GNSS-R coherent reflection detection algorithms using simulated and measured CYGNSS data. IEEE Trans. Geosci. Remote Sens. 61 https://doi.org/10.1109/TGRS.2023.3277411.

Lowe, S.T., LaBrecque, J.L., Zuffada, C., Romans, L.J., Young, L.E., Hajj, G.A., 2002. First spaceborne observation of an earth-reflected GPS signal. Radio Sci. 37 https://doi.org/10.1029/2000RS002539, 7–1–7–28.

Martín-Neira, M., 1993. A passive reflectometry and interferometry system (PARIS): application to ocean altimetry. Eur. Space Agency J. 17, 331–355.

Masters, D., Roberts, T.M., Chew, C., Lowe, S., McCleese, D., Tan, L., Ruf, C.S., Gleason, S., 2023. Sustainable signal of opportunity observations from the Muon small satellite constellation. In: Proc. of the 2023 IEEE IGARSS, Pasadena, USA, July 2023.

Morris, M., Chew, C., Reager, J.T., Shah, R., Zuffada, C., 2019. A novel approach to monitoring wetland dynamics using CYGNSS: everglades case study. Remote Sens. Environ. 233, 111417 https://doi.org/10.1016/j.rse.2019.111417.

Olthof, I., Rainville, T., 2022. Dynamic surface water maps of Canada from 1984 to 2019 landsat satellite imagery. Remote Sens. Environ. 279, 113121 https://doi.org/10.1016/j.rse.2022.113121.

Parkera, J., Boescha, H., McNortonc, J., Comyn-Platt, E., Gloore, M., Wilson, C., Chipperfield, M.P., Hayman, G.D., Bloom, A.A., 2018. Evaluating year-to-year anomalies in tropical wetland methane emissions using satellite CH4 observations. Remote Sens. Environ. 211, 261–275. https://doi.org/10.1016/j.rse.2018.02.011.

Pekel, J.F., Cottam, A., Gorelick, N., Belward, A.S., 2016. High-resolution mapping of global surface water and its long-term changes. Nature 540 (7633), 418–422. https://doi.org/10.1038/nature20584.

Pickens, A.H., Hansen, M.C., Stehman, S.V., Tyukavina, A., Potapov, P., Zalles, V., Higgins, J., 2022. Global seasonal dynamics of inland open water and ice. Remote Sens. Environ. 272, 112963 https://doi.org/10.1016/j.rse.2022.112963.

Pickensa, A.H., Hansena, M.C., Hancherb, M., Stehmanc, S.V., Tyukavinaa, A., Potapova, P., Marroquina, B., Sherani, Z., 2020. Mapping and sampling to characterize global inland water dynamics from 1999 to 2018 with full landsat time-series. Remote Sens. Environ. 243, 111792 https://doi.org/10.1016/j.rse.2020.111792.

Pierdicca, N., Comite, D., Camps, A., Carreno-Luengo, H., Cenci, L., Clarizia, M.P., Costantini, F., Dente, L., Guerriero, L., Mollfulleda, A., Paloscia, S., Park, H., Santi, E., Zribi, M., Floury, N., 2021. The potential of spaceborne GNSS reflectometry for soil moisture, biomass, and freeze–thaw monitoring: summary of a European Space Agency-funded study. IEEE Geosci. Remote Sens. Mag. 10 (2), 8–38. https://doi.org/10.1109/MGRS.2021.3115448.

Ruf, C.S., Lyons, A., Unwin, M., Dickinson, J., Rose, R., Rose, D., Vincent, M., 2013. CYGNSS: enabling the future of hurricane prediction [remote sensing satellites]. IEEE Geosci. Remote Sens. Mag. 1 (2), 52–67. https://doi.org/10.1109/MGRS.2013.2260911.

Ruf, C.S., Atlas, R., Chang, P.S., Clarizia, M.P., Garrison, J.L., Gleason, S., Katzberg, S.J., Jelenak, Z., Johnson, J.T., Majumdar, S.J., O'brien, A., Posselt, D.J., Ridley, A.J., Rose, R.J., Zavorotny, V.U., 2015. New Ocean winds satellite mission to probe hurricanes and tropical convection. Bull. Am. Meteorol. Soc. 97 (3), 385–395. https://doi.org/10.1175/BAMS-D-14-00218.1.

Ruf, C.S., Chew, C., Lang, T., Morris, M.G., Nave, K., Ridley, A., Balasubramaniam, R., 2018. A new paradigm in earth environmental monitoring with the CYGNSS small satellite constellation. Sci. Rep. 8 (1), 1–13. https://doi.org/10.1038/s41598-018-27127-4.

Ruf, C.S., Balasubramaniam, R., Carreno-Luengo, H., McKague, D., 2023. The NASA CYGNSS mission. In: Proc. of the 2023 IEEE IGARSS, Pasadena, USA, July 2023.

Russo, I.M., di Bisceglie, M., Galdi, C., Lavalle, M., Zuffada, C., 2021. Entropy-based coherence metric for land applications of GNSS-R. IEEE Trans. Geosci. Remote Sens. 60, 5613413. https://doi.org/10.1109/TGRS.2021.3125858.

Santi, E., Paloscia, S., Pettinato, S., Fontanelli, G., Clarizia, M.P., Comite, D., Dente, L., Guerriero, L., Pierdicca, N., Floury, N., 2020. Remote sensing of forest biomass using GNSS reflectometry. IEEE J. Sel. Top. Geosci. Remote Sens. 13, 2351–2368. https://doi.org/10.1109/JSTARS.2020.2982993.

Unwin, M., Pierdicca, N., Cardellach, E., Rautiainen, K., Foti, G., Blunt, P., Guerriero, L., Santi, E., Tossaint, M., 2021. An introduction to the HydroGNSS GNSS reflectometry remote sensing mission. IEEE J. Sel. Top. Appl. Earth Obs. Remote Sens. 14, 6987–6999. https://doi.org/10.1109/JSTARS.2021.3089550.

Vanderhoof, M.K., Alexander, L., Christensen, J., Solvik, K., Nieuwlandt, P., Sagehorn, M., 2023. High-frequency time series comparison of sentinel-1 and sentinel-2 satellites for mapping open and vegetated water across the United States (2017–2021). Remote Sens. Environ. 288 (113498), 2023. https://doi.org/10.1016/j.rse.2023.113498.

Wickert, J., Cardellach, E., Martín-Neira, M., Bandeiras, J., Bertino, L., Andersen, O.B., Camps, A., Catarino, N., Chapron, B., Fabra, F., Floury, N., Foti, G., Gommenginger, C., Hatton, J., Høeg, P., Jäggi, A., Kern, M., Lee, T., Li, Z., Park, H., Pierdicca, N., Ressler, G., Rius, A., Rosello, J., Saynisch, J., Soulat, F., Shum, C.K., Semmling, M., Sousa, A., Xie, J., Zuffada, C., 2016. GEROS-ISS: GNSS reflectometry, radio occultation, and scatterometry onboard the International Space Station. IEEE J. Sel. Top. Geosci. Remote Sens. 9 (10), 4552–4581. https://doi.org/10.1109/JSTARS.2016.2614428.

Winkelried, J., Ruf, C., Gleason, S., 2023. Spatial and temporal sampling properties of a large GNSS-R satellite constellation. MDPI Remote Sens. 12 (3), 333. https://doi.org/10.3390/rs15020333.

Zavorotny, V.U., Gleason, S., Cardellach, E., Camps, A., 2014. Tutorial on remote sensing using GNSS bistatic radar of opportunity. IEEE Geosci. Remote Sens. Mag. 2 (4), 8–45. https://doi.org/10.1109/MGRS.2014.2374220.

Zhang, J., Morton, J., Wang, Y., Roesler, C.J., 2022. Mapping surface water extents using high-rate coherent spaceborne GNSS-R measurements. IEEE Trans. Geosci. Remote Sens. 60 https://doi.org/10.1109/TGRS.2022.3218254.